JOURNAL OF PROPULSION AND POWER
Vol. 14, No. 3, May–June 1998

# Transition Characteristics of Flowfield in a Simulated Solid-Rocket Motor

Tong-Miin Liou,* Wan-Yih Lien,† and Po-Wen Hwang†
*National Tsing Hua University, Hsinchu 30043, Taiwan, Republic of China*

**The flow characteristics in a two-dimensional porous-walled duct simulating a solid-propellant rocket motor are numerically computed to investigate the effects of viscosity, compressibility, and inflow turbulence ($\sigma_w$) on the flow transitions. The finite volume technique is used to solve the time-dependent compressible Navier–Stokes equations with a subgrid-scale turbulence model, and the numerical fluxes are computed using a modified Godunov scheme. In addition to computed axial mean velocity and turbulence intensity profiles, the axial variations of skin friction coefficient and the transverse location of peak turbulence intensity are used to identify the mean-flow transition and turbulence-intensity transition, respectively. In particular, a new way of identifying turbulence-intensity transition by the use of the power spectrum of velocity fluctuations is presented for the first time in the present study. The minimum centerline Mach number for the onset of mean-flow transition is obtained as the compressibility is considered alone. The critical values of $\sigma_w$ for the onset of turbulence-intensity transition and mean-velocity transition advance as well as for the concurrence and delay between the two transitions are also determined to illustrate why some researchers could observe only a single transition whereas others observed two transitions.**

## Nomenclature

$C_f$ = skin friction coefficient, $\tau_w/(\bar{\rho}\tilde{u}^2/2)$
$c_k$ = model constant
$c_s$ = Smagorinsky constant
$D$ = near-wall damping function
$\hat{E}$ = filtered total energy per unit volume, $\bar{p}/(\gamma - 1) + 0.5\bar{\rho}(\tilde{u}^2 + \tilde{v}^2)$, J/m$^3$
$\boldsymbol{F}$ = convective flux vector in $x$ direction of Navier–Stokes equations
$G$ = spatial filter function
$\boldsymbol{G}$ = convective flux vector in $y$ direction of Navier–Stokes equations
$g$ = flow variable
$h$ = duct half-height, m
$I$ = turbulence intensity, $\langle \tilde{u}'''\tilde{u}''' + \tilde{v}'''\tilde{v}''' \rangle^{1/2}$, m/s
$I_p$ = peak value of turbulence intensity, m/s
$I_w$ = injected-fluid turbulence intensity at porous surface, m/s
$k$ = turbulence kinetic energy, m$^2$/s$^2$
$k_s$ = subgrid turbulent kinetic energy, m$^2$/s$^2$
$L$ = duct length, m
$M$ = mean cross-sectional-averaged Mach number
$M_{CL}$ = mean centerline Mach number
$Pr_s$ = subgrid-scale Prandtl number
$p$ = pressure, N/m$^2$
$\boldsymbol{Q}$ = conservation variables vector of Navier–Stokes equations
$q_s$ = subgrid-scale heat flux, W/m$^2$
$S_{ij}$ = strain rate tensor, $\frac{1}{2}[(\partial u_i/\partial x_j) + (\partial u_j/\partial x_i)] - \frac{1}{3}\delta_{ij}(\partial u_k/\partial x_k)$
$s$ = streamline coordinate
$T$ = temperature, K
$t$ = time coordinate, s
$u$ = velocity in $x$ direction, m/s
$u_\tau$ = friction velocity, $\sqrt{\tau_w/\bar{\rho}}$, m/s
$u^+$ = $\tilde{u}/u_\tau$
$v$ = velocity in $y$ direction, m/s
$v_w$ = blowing or injection velocity, m/s
$x, y$ = Cartesian coordinates
$\boldsymbol{x}$ = position vector
$y_p$ = location of $I_p$ from porous wall
$y^+$ = dimensionless distance from walls, $yu_\tau/\nu$
$\gamma$ = specific heats ratio
$\Delta$ = filter width
$\delta_{ij}$ = Kronecker delta function
$\varepsilon$ = dissipation rate of turbulence kinetic energy, m$^2$/s$^3$
$\boldsymbol{\zeta}$ = dummy variable
$\kappa$ = thermal conductivity, W/(m·K)
$\mu$ = dynamic viscosity, kg/(m·s)
$\nu$ = kinematic viscosity, m/s$^2$
$\nu_s$ = subgrid kinematic viscosity, m/s$^2$
$\rho$ = density, kg/m$^3$
$\sigma$ = $I/\tilde{v}_w$, nondimensional turbulence intensity
$\sigma_w$ = surface-generated pseudoturbulence, $I_w/\tilde{v}_w$
$\tau$ = viscous shear stress, N/m$^2$
$\tau_s$ = subgrid-scale shear stress, N/m$^2$
$\tau_w$ = shear stress at wall, N/m$^2$
$\Omega$ = flow domain

*Subscripts*
$e$ = exit plane
$h$ = head end
$w$ = blowing wall

*Superscripts*
$'$ = subgrid component
$''$ = mass-weighted subgrid component
$'''$ = temporally fluctuating value of variables
$-$ = spatially filtered quantity
$\sim$ = mass-weighted spatially filtered quantity
$\langle\ \rangle$ = time-averaged quantity

Received June 10, 1996; revision received July 19, 1997; accepted for publication Oct. 18, 1997. 

*Professor, Department of Power Mechanical Engineering.
†Graduate Student, Department of Power Mechanical Engineering.

## Introduction

AN important issue in designing a solid-propellant rocket motor (SRM) is the transitional behavior of the mean-

**Table 1 Summary of previous experiments regarding mean-flow and turbulence-intensity transitions**

| References | Wall injection | $L$, cm | $L/h$ or $L/R$ | $\tilde{v}_w$, m/s | $M_{G_x}$ | Mean-flow transition | Turbulence-intensity transition |
|---|---|---|---|---|---|---|---|
| 2 | Uniform | 74.88 | 15.5 | 1.18 | 0.16 | No | Yes |
| 3 | Uniform | 30 | 20 | 2 | 0.12 | No | Yes |
| 6 | Uniform | 48 | 48 | 3.1 | 1.15 | Yes | Yes |
| 10 | Uniform | 146 | 28.6 | 1.18 | 0.28 | Yes | Yes |
| 17 | Nonuniform | 42 | 42 | 0–7.9 | 0.27 | Yes | Yes |
| 7 | Nonuniform | 41.7 | 42.7 | 0–3.5 | 0.35 | Yes | Yes |

flow velocity and turbulence quantities. This is because the ballistics prediction is affected by the erosive burning behavior of the solid propellant, which, in turn, is related to the transitional behavior of the propellant burning-induced flowfield. This paper is concerned with the transition characteristics of flowfield in a simulated SRM.

A detailed literature survey was given in our previous work.[1] In the following, therefore, only the most relevant works will be addressed and some of them are listed in Table 1. Experiments of Dunlap et al.[2] and Yamada et al.[3] showed the laminar-like similar velocity profile[4,5]

$$\langle \tilde{u}/\tilde{u}_c \rangle = \sin\left[\frac{\pi}{2}\left(\frac{y}{h}\right)^{n+1}\right] \tag{1}$$

where $n = 0$ represents a planar flow, and $n = 1$ represents an axisymmetric flow that persists in the entire test section (no mean-flow transition); however, the turbulence-intensity peak shifts toward the porous wall as the axial distance increases (turbulence-intensity transition). The turbulence-intensity transition and mean-flow transition, i.e., the mean-velocity profile starts to deviate from the similar velocity profile described by Eq. (1), have been observed to coexist at the same axial location in the experimental investigations of Traineau et al.[6] Tsai[7] further experimentally demonstrated that the turbulence-intensity transition could occur spatially earlier than the mean flow transition.

As for the two-dimensional theoretical analysis, Beddini[8] used a full Reynolds stress model to study the effects of surface-generated pseudoturbulence on the mean-flow transition. An attempt to predict the occurrence of mean-flow transition was not attained within the channel length used in the experiment of Yamada et al.[3] Sabnis et al.[9] also made an attempt to simulate the flowfields and transitions investigated by Dunlap et al.[10] and Traineau et al.,[6] using a low Reynolds number $k$-$\varepsilon$ turbulence model. The emphasis is on the near-wall damping factor in the turbulence model. Balakrishnan et al.[11] derived a single integral equation to study the flow in a porous duct and showed that the compressibility phenomenon is a candidate for causing the mean-flow transition. Liou et al.[12] both computationally and experimentally displayed an earlier initiation of turbulence-intensity transition than mean-flow transition. In the computation of Ref. 12, the two-dimensional Navier–Stokes equations were solved directly using the Godunov method without turbulence models.

The preceding surveyed works have provided valuable information regarding the flow transition phenomenon in porous channels. However, it is obvious that more studies of transition characteristics are needed. In particular, the interrelationship of the mean-flow and turbulence-intensity transitions, such as simultaneous transitions of both mean velocity and turbulence intensity or the presence of the delay between the two transitions, and the significance of turbulence level in the injected fluid on the transitions have not received much attention yet, to the authors' knowledge. It is this fact that motivates the present study. In addition, the power spectrum role of velocity fluctuations in the aforementioned transitions has not been explored in the past and is, therefore, examined in the present study.

## Theoretical Analysis

### Governing Equations

In the current simulations the flow variables are decomposed into a large-scale (or resolved) part that can be solved explicitly and a subgrid-scale (SGS) part that is modeled with a subgrid-scale model. The following filtering operation

$$\bar{g}(\boldsymbol{x}) = \int_\Omega G_\Delta(\boldsymbol{x} - \boldsymbol{\zeta}) g(\boldsymbol{\zeta})\, \mathrm{d}\zeta \tag{2}$$

decomposes a variable $g$ into a large-scale component $\bar{g}$ and a subgrid-scale component $g'$, which accounts for the scales not resolved by $\Delta$:

$$g = \bar{g} + g' \tag{3}$$

A mass-weighted filter that simplifies the mathematical expressions for compressible flow simulations is defined by

$$\tilde{g} = \overline{\rho g}/\bar{\rho} \tag{4}$$

This implies a second decomposition of $g$:

$$g = \tilde{g} + g'' \tag{5}$$

Assuming that there are no external heat additions and body forces, the filtered forms of compressible mass, momentum, and total energy equations with the Smagorinsky SGS eddy viscosity model[13] in two-dimensional Cartesian coordinates (Fig. 1) can be respectively written as

$$\frac{\partial \bar{\rho}}{\partial t} + \frac{\partial}{\partial x}(\bar{\rho}\tilde{u}) + \frac{\partial}{\partial y}(\bar{\rho}\tilde{v}) = 0 \tag{6}$$

$$\frac{\partial}{\partial t}(\bar{\rho}\tilde{u}) + \frac{\partial}{\partial x}(\bar{\rho}\tilde{u}\tilde{u} - \bar{\tau}_{xx} - \tau_{s_{xx}}) + \frac{\partial}{\partial y}(\bar{\rho}\tilde{u}\tilde{v} - \bar{\tau}_{xy} - \tau_{s_{xy}}) = 0 \tag{7}$$

$$\frac{\partial}{\partial t}(\bar{\rho}\tilde{v}) + \frac{\partial}{\partial x}(\bar{\rho}\tilde{v}\tilde{u} - \bar{\tau}_{yx} - \tau_{s_{yx}}) + \frac{\partial}{\partial y}(\bar{\rho}\tilde{v}\tilde{v} - \bar{\tau}_{yy} - \tau_{s_{yy}}) = 0 \tag{8}$$

$$\frac{\partial \hat{E}}{\partial t} + \frac{\partial}{\partial x}\left(\hat{E}\tilde{u} - \overline{u\tau}_{xx} - \overline{v\tau}_{yx} - \tilde{u}\tau_{s_{xx}} - \tilde{v}\tau_{s_{yx}} - \frac{\kappa \partial \bar{T}}{\partial x} - q_{s_x}\right) + \frac{\partial}{\partial y}\left(\hat{E}\tilde{v} - \overline{u\tau}_{xy} - \overline{v\tau}_{yy} - \tilde{u}\tau_{s_{xy}} - \tilde{v}\tau_{s_{yy}} - \frac{\kappa \partial \bar{T}}{\partial y} - q_{s_y}\right) = 0 \tag{9}$$

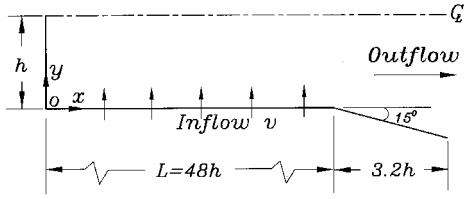


**Fig. 1 Schematic diagram of simulated SRM model with uniform wall injection ($h$ = 1 cm).**

where viscous stresses $\tau_{ij}$ are defined as

$$\tau_{xx} = -p + 2\mu\left[\frac{\partial u}{\partial x} - \frac{1}{3}\left(\frac{\partial u}{\partial x} + \frac{\partial v}{\partial y}\right)\right]$$

$$\tau_{yy} = -p + 2\mu\left[\frac{\partial v}{\partial y} - \frac{1}{3}\left(\frac{\partial u}{\partial x} + \frac{\partial v}{\partial y}\right)\right]$$

$$\tau_{xy} = \tau_{yx} = \mu\left(\frac{\partial u}{\partial y} + \frac{\partial v}{\partial x}\right)$$

The two terms $\tau_{s_{ij}}$ and $q_{s_j}$ are the SGS stresses and heat fluxes, respectively, and can be modeled as

$$\tau_{s_{xx}} = \bar{\rho}(\tilde{u}\tilde{u} - \tilde{u}\tilde{u}) = 2\bar{\rho}\nu_s\left[\frac{\partial \tilde{u}}{\partial x} - \frac{1}{3}\left(\frac{\partial \tilde{u}}{\partial x} + \frac{\partial \tilde{v}}{\partial y}\right)\right] - \frac{2}{3}\bar{\rho}k_s$$

$$\tau_{s_{yy}} = \bar{\rho}(\tilde{v}\tilde{v} - \tilde{v}\tilde{v}) = 2\bar{\rho}\nu_s\left[\frac{\partial \tilde{v}}{\partial y} - \frac{1}{3}\left(\frac{\partial \tilde{u}}{\partial x} + \frac{\partial \tilde{v}}{\partial y}\right)\right] - \frac{2}{3}\bar{\rho}k_s$$

$$\tau_{s_{xy}} = \tau_{s_{yx}} = \bar{\rho}(\tilde{u}\tilde{v} - \tilde{u}\tilde{v}) = \bar{\rho}\nu_s\left(\frac{\partial \tilde{u}}{\partial y} + \frac{\partial \tilde{v}}{\partial x}\right)$$

$$q_{s_x} = \bar{\rho}c_p(\tilde{T}\tilde{u} - \tilde{T}\tilde{u}) = \frac{c_p\bar{\rho}\nu_s}{Pr_s}\frac{\partial \tilde{T}}{\partial x}$$

$$q_{s_y} = \bar{\rho}c_p(\tilde{T}\tilde{v} - \tilde{T}\tilde{v}) = \frac{c_p\bar{\rho}\nu_s}{Pr_s}\frac{\partial \tilde{T}}{\partial y}$$

where $\nu_s$ and $k_s$, prescribed by the Smagorinsky model are

$$\nu_s = (c_s D\Delta)^2\left(2S_{ij}\frac{\partial \tilde{u}_i}{\partial x_j}\right)^{1/2}, \qquad k_s = \nu_s^2/(c_k\Delta)^2$$

In the preceding equations, $c_s$ (=0.15) and $c_k$ (=0.094) are model constants, $\Delta$ is the average size of the computational cell, and $D$ is expressed as

$$D = 1 - \exp[-(y^+)^3/26^3]$$

Equations (6–9) can be put into the following general form:

$$\frac{\partial \boldsymbol{Q}}{\partial t} + \frac{\partial \boldsymbol{E}}{\partial x} + \frac{\partial \boldsymbol{G}}{\partial y} = 0 \tag{10}$$

### Numerical Method

The finite volume technique is adopted in the present code. The conservation variables $\bar{\rho}$, $\bar{\rho}\tilde{u}$, $\bar{\rho}\tilde{v}$, and $\hat{E}$ are calculated at the center of each computational cell, whereas flux vectors $\boldsymbol{F}$ and $\boldsymbol{G}$ in Eq. (10) are calculated at the cell edges using Godunov's scheme.[14] Godunov used characteristic information so that the Riemann problem could be solved forward in time. From the solution of the Riemann problem, the numerical flux at the cell edges can thus be calculated. To improve the order of spatial accuracy of Godunov's original scheme, the piecewise initial states to the left and right of the cell edges are obtained by a second-order extrapolation[15] in the present work.

### Boundary and Initial Conditions

At the head end of the channel no-slip, zero normal pressure gradient, and an adiabatic wall conditions are used for the primitive variables $\tilde{u}$, $\tilde{v}$, $\bar{p}$, and $\bar{\rho}$, respectively. Along the centerline of the channel, the symmetry conditions are applied for all primitive variables. Characteristic-based boundary conditions are enforced on the inflow and outflow boundaries. At the inflow, both mass flux and energy flux are kept constant with $\tilde{u} = 0$ specified because there are three incoming characteristics and one outgoing characteristic for the subsonic inlet velocity. Mathematically, they are

$$\bar{\rho}\tilde{v} = c_1 \tag{11}$$

$$[\gamma/(\gamma - 1)]\bar{p}/\bar{\rho} + \tfrac{1}{2}(\tilde{u}^2 + \tilde{v}^2) = c_2 \tag{12}$$

$$\tilde{u} = 0 \tag{13}$$

where $c_1$ and $c_2$ are constants to be determined by the measured initial conditions. The primitive variables at the inflow can thus be determined by incorporating Eqs. (11–13) with the linear acoustic wave equation of the outgoing characteristic. At the expander exit, there are four outgoing characteristics for the supersonic outlet velocity, and the outflow boundary conditions need not be specified. Specification of the initial conditions is based on the experimental measurements of Traineau et al.[6]: $\tilde{v}_w$ = 3.1 m/s, $\bar{p}$ = 314,253 N/m$^2$, and $T$ = 260 K.

### Grid Independence

A detailed grid-independence test in terms of mean velocity and turbulence intensity profiles throughout the flowfield were reported in our previous work,[1] and a 642 × 52 system of nonuniform grids clustered at the porous wall and the beginning of the expander was found to be appropriate. The corresponding smallest axial and transverse resolutions are $3 \times 10^{-3}$ mm at the beginning of the expander and $10^{-3}$ mm near the porous wall, respectively. The latter provides viscous sublayer resolution. The Courant number was fixed at 0.6 to guarantee numerical stability, and to advance the code in time it properly results in a temporal resolved scale of $1.7 \times 10^{-9}$ s. The time-averaged results extracted from the fluctuating field over the time interval ($4.2 \leq t \leq 12.6$ ms) are found to attain the asymptotic converged solutions.

It is important to examine whether the large, energy-containing scales are appropriately resolved by the present code. Also, note that in the large-eddy simulation, the cutoff frequency or wave number resolved by the grid size needs to be in the inertial subrange. The spectra of streamwise fluctuations at two locations near the porous wall for the case without using SGS turbulence models are shown in Fig. 2. It is observed that the present numerical solutions can resolve the spectrum frequency ranging up to the inertial subrange (slope = −5/3); the large eddy characteristics are thus appropriately captured and the introduction of a normal SGS model therefore does not change the cutoff frequency and, in turn, the grid sensitivity.

The unresolved eddy characteristics (eddies with frequency beyond the cutoff frequency) are modeled by the Smagorinsky SGS model. The necessity of adopting an SGS model in the present study is addressed later in this paper. In general, computations with and without an SGS turbulence model give good predictions of the mean velocity and turbulence-intensity field, as will be and have been demonstrated by our present and previous studies,[1] respectively. However, although the numerical diffusion for the case without the SGS model behaves similar to a normal SGS model, it is not the primary mechanism by which energy of the resolved scales is dissipated. A normal SGS model plays a role in that dissipation. The preceding difference in dissipating the energy transferred from the resolved scales to the unresolved scales can be demonstrated in Fig. 2. A similar demonstration for the mixing layers can

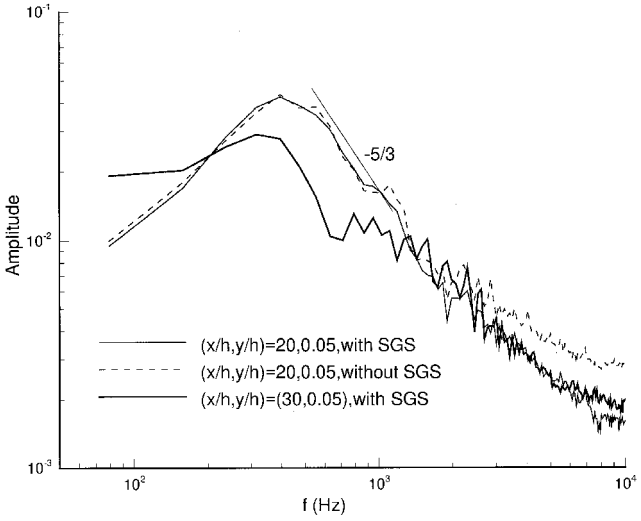


**Fig. 2 Spectra of axial velocity fluctuations at two locations near porous wall ($\tilde{v}_w$ = 3.1 m/s).**

be found in the work of Ragab and Sheen.[16] Figure 2 clearly indicates the pile up of energy at high frequencies of the resolved field for the case without the SGS model. Consequently, it is necessary to introduce an SGS model in the present work.

## Results and Discussion

### Mean Velocity and Turbulence Intensity

In our previous work,[1] without using the SGS model, the computed mean velocity profiles, turbulence intensity distributions, and static pressure contours throughout the whole flowfield had been compared with the experimental data measured by Traineau et al.,[6] and good agreement was achieved. In general, the prediction of turbulence intensity distribution is more critical. A comparison of predicted turbulence intensity distributions by the present code with and without using the SGS model with the data measured by Traineau et al.[6] is provided in Fig. 3. As one can see, a slightly better prediction is attained by the case with the SGS model. Both computational and experimental results all depict the shifts in turbulence intensity profiles, from a mild and broad maximum to a sharp and high peak, with the transverse location $y_p$ of the peak turbulence intensity in a given profile decreased with increasing $x/h$. A further investigation of the influence of the turbulence intensity of the injected fluid at the porous surface $\sigma_w(=I_w/\tilde{v}_w)$ on the $y_p$ shift will be provided later in the text.

### Effect of Viscosity and Compressibility

The derivation of similar velocity profiles, Eq. (1), for the laminar-like mean flowfield in laterally burning solid-propellant rocket motors is based on the assumption that the flow is laminar, inviscid, and incompressible. The similarity breaks down as the transition phenomenon occurs, because the flow is actually turbulent and, in particular, compressible after the onset of mean-flow transition. An exploration of the viscosity, compressibility, and inlet turbulence effects will therefore be helpful for clarifying the transition characteristics.

The viscous effect on the streamwise evolution of the axial mean velocity is depicted in terms of a comparison of the computed results obtained by solving the Euler and Navier–Stokes equations. Figure 4 reveals no difference found in these two computed results. Similarly, the viscous effect has almost no influence on the mean-flow transition, as can be observed from a comparison of the axial variations of skin friction coefficient $C_f$ in Fig. 5 computed from the Euler and Navier–Stokes equations. In addition, because the porous surface-generated turbulence $I_w$ (or $\sigma_w$) is not accounted for in computing Fig. 5, the turbulence effect is further excluded from Fig. 5,

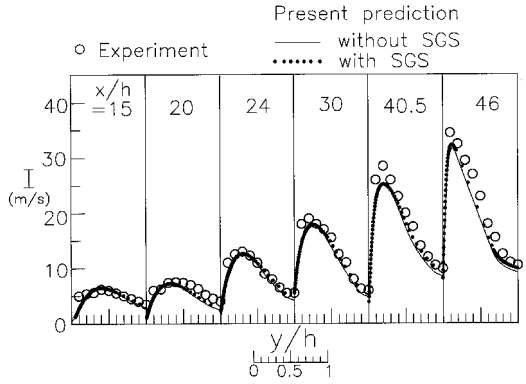


**Fig. 3 Turbulence-intensity profiles at various axial stations computed with and without a SGS turbulence model ($\tilde{v}_w$ = 3.1 m/s).**

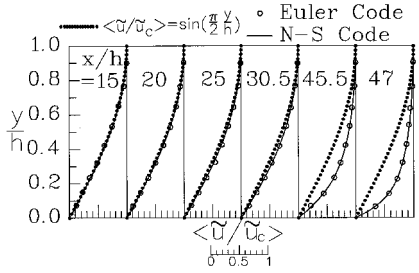


**Fig. 4 Normalized axial mean-velocity profiles at various axial stations computed by Euler and Navier–Stokes equations ($\tilde{v}_w$ = 3.1 m/s).**

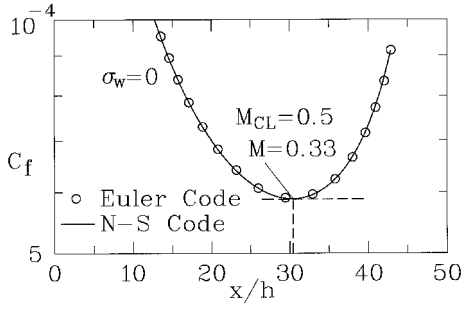


**Fig. 5 Axial variation of skin friction coefficient computed by Euler and Navier–Stokes equations ($\tilde{v}_w$ = 3.1 m/s).**

which is thus able to show the compressibility effect on the mean-flow transition alone. The mean-flow transition occurs at $x/h$ = 30.5, the minimum of the $C_f$ curve. Downstream from the transition station, $C_f$ starts to increase with increasing $x/h$, and the axial mean-flow velocity departs from the laminar similar solution with an increase in flatter transverse profiles, as shown in Fig. 4. At the mean-flow transition station the mean centerline Mach number and the mean cross-sectional averaged Mach number are 0.5 and 0.33, respectively, which propose the minimum centerline mean velocity and bulk mean velocity for the onset of the mean-flow transition as the compressibility effect is considered alone.

The physical picture of compressibility effects can be demonstrated in terms of fractional mean density variation and Mach number contours in Fig. 6. Clearly, there is a change in the mean density profile that requires a modification in the mean velocity profile (Fig. 4) to conserve mass flow. Figure 6 shows that as the flow accelerates from the head end to the channel exit, the centerline Mach number at $x/h$ = 30.5 has been increased up to 0.5 and the fractional mean density variation has attained a value as high as 12% to trigger the mean-flow transition.

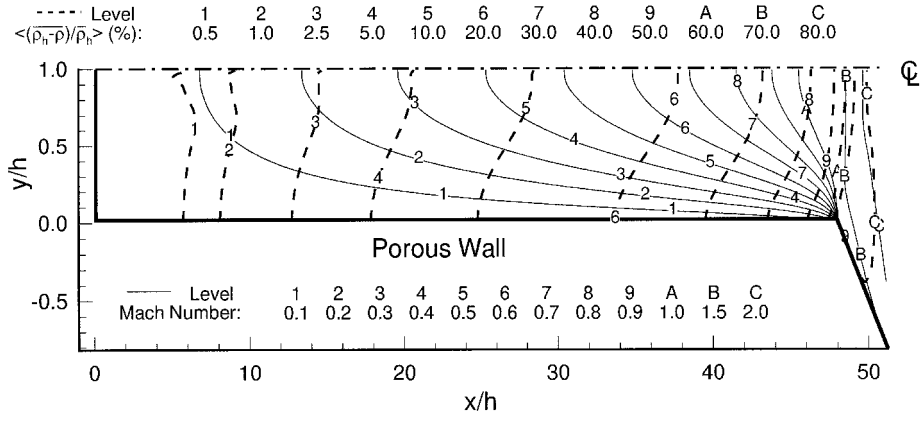


**Fig. 6 Contour plots of fractional mean density variation and Mach number distribution ($\tilde{v}_w$ = 3.1 m/s).**

### Effect of Turbulence ($\sigma_w$) in Injected Fluid

It is commonly accepted that inlet turbulence in an SRM can be generated through roughness or porosity of the propellant. The laminar-flow assumption in fact does not exist, although the mean-flow profiles before transition can be simulated by the laminar-like similar solution caused by a strongly favorable axial pressure gradient. Because the flow in an SRM is actually turbulent, it is instructive to examine the effect of $\sigma_w$ on the mean-flow transition. Figure 7 shows that for $0 \leq \sigma_w \leq 0.3$, the mean-flow transition always occurs at $x/h = 30.5$ where, as illustrated before, the mean centerline Mach number has attained the critical value for mean-flow transition provoked by compressibility. $\sigma_w$ has a pronounced effect on the axial station where mean-flow transition occurs only as $\sigma_w \geq 0.3$. Beyond $\sigma_w = 0.3$, the mean-flow transition advance increases and the corresponding transition critical centerline Mach number decreases with increasing $\sigma_w$. In other words, as far as the mean-flow transition is concerned, the compressibility plays a dominant role as $0 \leq \sigma_w \leq 0.3$, whereas the turbulence intensity level at the porous surface becomes the controlling factor as $\sigma_w \geq 3$. In contrast to the effect of $\sigma_w$ on the mean-flow transition, Fig. 8 shows that the turbulence-intensity transition is much more sensitive to the level of $\sigma_w$. It only needs a value of $\sigma_w$ as low as 0.01 to trigger the turbulence-intensity transition, i.e., the peak turbulence intensity begins to shift toward the porous wall as $\sigma_w \geq 0.01$. The turbulence-intensity transition advance also increases with increasing $\sigma_w$.

### Comparison Among Various Works

The transition characteristics can also be elucidated by comparing various measured cross-sectional nondimensional turbulence-intensity $\sigma$ profiles for the uniform wall injection cases listed in Table 1, although $\sigma_w$ is not indicated in these experimental works, with the present results computed at critical values of $\sigma_w$. This is shown in Fig. 9, where all profiles are taken from $x/L = 0.5$ because all works have measurements made at this axial station. The experimental data of Tsai[7] and Tsai and Liou[17] are not included because the computed results presented in this section are obtained under uniform wall injection. It is seen that the $\sigma$ profiles measured by Dunlap et al.[2] and Yamada et al.[3] are located below the computed $\sigma$ profile of $\sigma_w = 0.3$ (minimum value for mean-flow transition advance), whereas the experimental data of Traineau et al.[6] and Dunlap et al.[10] exceed the computed results of $\sigma_w = 0.3$. Consequently, Fig. 9 clearly demonstrates why in the works of Dunlap et al.[2] and Yamada et al.[3] the mean-flow transition does not occur, because their $\sigma_w$ values inferred from the comparison in Fig. 9 are below 0.3 and their exit centerline Mach numbers are 0.16 and 0.12, respectively, as shown in Table 1, which do not exceed 0.5, the aforementioned compressibility critical value. Conversely, the $\sigma_w$ values of Traineau et al.[6] and Dunlap et al.[10] exceed 0.3, which leads to the mean-flow transition advance (Fig. 7) and, in turn, the decrease of the transition Mach number. For the case of Dunlap et al.,[10] the exit centerline Mach number does not exceed 0.5 and their mean-flow transition is thus principally provoked by the $\sigma_w$ level, whereas for the case of Traineau et al.,[6] the exit centerline Mach number is 1.15 and the mean-flow transition is agitated by both the $\sigma_w$ level and compressibility. As for the turbulence-intensity transition, Fig. 9 depicts that all of the experimental $\sigma_w$ values exceed 0.01 (minimum value for turbulence-intensity transition), which is consistent with the fact that the turbulence-intensity transition is indeed observed in these experiments. Furthermore, the experimental $\sigma_w$ curve of Traineau et al.[6] is adjacent to (or slightly higher than) $\sigma_w = 0.9$ in Fig. 9. Both Figs. 7 and 8 subsequently indicate the occurrences of the turbulence-intensity transition and the mean-flow transition at about $x/h = 20$, which agrees with the fact that in the work

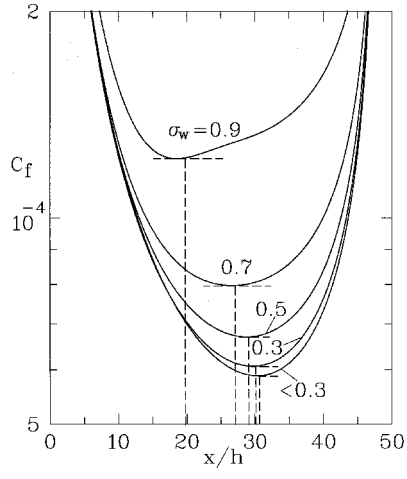


**Fig. 7 Axial variation of skin friction coefficient with various values of $\sigma_w$ ($\tilde{v}_w$ = 3.1 m/s).**

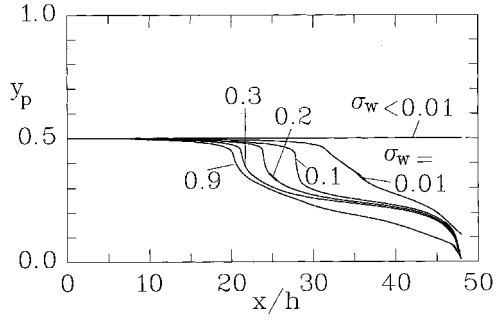


**Fig. 8 Axial variation of transverse location of peak turbulence intensity with various values of $\sigma_w$ ($\tilde{v}_w$ = 3.1 m/s).**

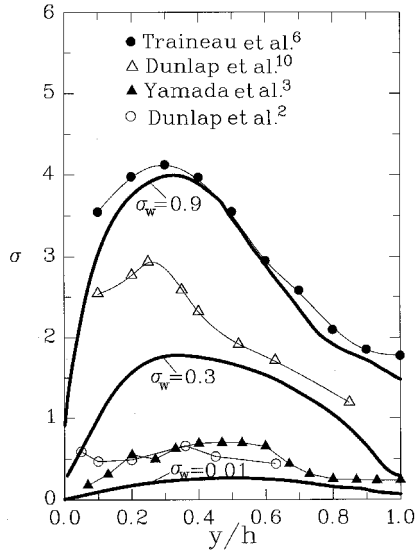


**Fig. 9 Comparison of computed normalized turbulence-intensity profiles with measured data at $x/L = 0.5$.**

of Traineau et al.[6] the mean-flow and turbulence-intensity transitions occur at the same axial location of about $x/h = 20$. In contrast, the $\sigma_w$ value of Dunlap et al.[10] is between $\sigma_w = 0.3$ and 0.9 of Fig. 9. In addition, the $\sigma_w = 0.3$ and 0.9 curves are closer in Fig. 8 than in Fig. 7, which suggests an onset of the turbulence-intensity transition ahead of that of the mean-flow transition.

### Instantaneous Streaklines and Pathlines Visualizations

In experimental flow visualization a smoke-tracer method is often used to observe the instantaneous flow structure. To numerically simulate the smoke flow visualization, maker particles are introduced into the flowfield at $t = 4.2$ ms, when the computation reaches convergence, with every time interval of $\Delta t = 0.021$ ms from 28 axial positions along the porous wall ($y/h = 0$) until $t = 11.34$ ms, and from five transverse positions along a line ($x/h = 0.1$) adjacent to the head end ($x/h = 0$) until $t = 8.82$ ms. The location of each released particle is followed using the computed velocity field and a fourth-order Runge–Kutta scheme in time. Figures 10 and 11 depict the results. All of the streaklines are rather smooth and the streaklines released from the same location at different times fall into the same single curve; an observation indicates that the flow is steady in the mean velocity field. The steady flow condition can also be verified from the overlap of streaklines and pathlines, i.e., particles traces, as evident from Fig. 10. Figure 10 also indicates that the $y/h$ distance where the streakline bends toward the downstream direction and the space between the streaklines decreases with increasing $x/h$, a message for flow acceleration toward the channel exit. Notice that the axial velocities in the vicinity of porous wall are very low, as indicated by the near perpendicular streaklines and pathlines adjacent to $y/h = 0$. Figure 11 further depicts the streaklines emitting from the $x/h = 0.1$ line. It is found that these particles actually first decelerate transversely toward the centerline with a slight tilt to the head end, that is, with a small negative axial velocity, and then accelerate axially toward the channel exit. The transverse deceleration is a result of the retardation by the symmetric condition with respect to the channel centerline. Only the particles released very near the centerline directly accelerate toward the channel exit.

### Instantaneous Timelines Visualization

Numerical passive particles, simulating hydrogen bubbles, are released periodically with a time interval of $\Delta t = 0.126$ ms from 56 positions along the porous wall to form the timelines shown in Fig. 12. The aforementioned transverse deceleration is clearly demonstrated again, as evidenced by the decreasing space between the timelines with increasing $y/h$. Additionally, most timelines, except those horizontal timelines near the channel centerline ($0.8 \leq y/h \leq 1.0$), have positive slopes, although all of the particles are injected into the channel from the porous wall with the same velocity. The result suggests that the transverse velocity of fluid flow in the channel increases with increasing $x/h$ for the region $0 < y/h < 0.8$, an observation not reported in the open literature. The reason is that there exists a favorable axial pressure gradient in the channel and, in turn, an increased streamline pressure gradient ($\partial \bar{p}/\partial s$) with increasing $x/h$. Around the channel centerline and near the channel exit, the divergence of timelines is a result of the effect of the downstream divergent expansion area ($x/h > 48$, Fig. 1).

Although the preceding numerical flow visualization techniques have provided some insights into the flow features, they fail to reveal the difference in flow structure before and after the previously discussed transition. We therefore turn our attention to the turbulence power spectrum given next.

### Velocity Power Spectrum

The computed near-wall power spectra of the axial-velocity fluctuations at locations $x/h = 4$, 8, 12, 16, 20, 24, 28, and 32 along $y/h = 0.05$ are plotted in Fig. 13. There is a distinct peak for each spectrum with a peak frequency of $395 \pm 20$ Hz. It is essential to note that the peak amplitude of the spectrum increases with increasing $x/h$ as the flow proceeds from the head end to $x/h = 20$; downstream of $x/h = 20$, however, it decreases with increasing $x/h$, as displayed in Fig. 14. Hence,

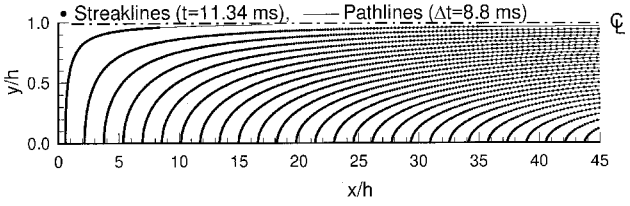


**Fig. 10 Instantaneous flow visualization of streaklines ($t = 11.34$ ms) and history of pathlines ($\Delta t = 8.8$ ms) emitting from the porous wall ($y/h = 0$; $\tilde{v}_w = 3.1$ m/s).**

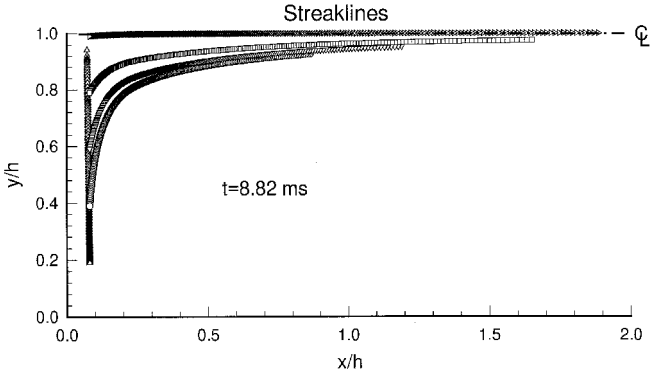


**Fig. 11 The instantaneous flow visualization of streaklines emitting near the head end ($x/h = 0.1$) at $t = 8.82$ ms ($\tilde{v}_w = 3.1$ m/s).**

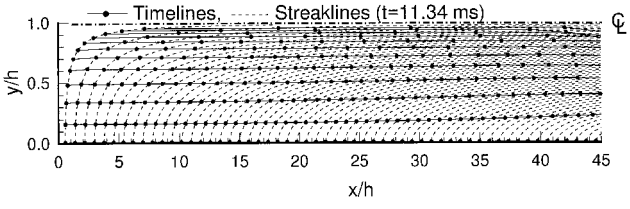


**Fig. 12 Instantaneous flow visualization of timelines emitting from the porous wall ($y/h = 0$) at $t = 11.34$ ms ($\tilde{v}_w = 3.1$ m/s).**

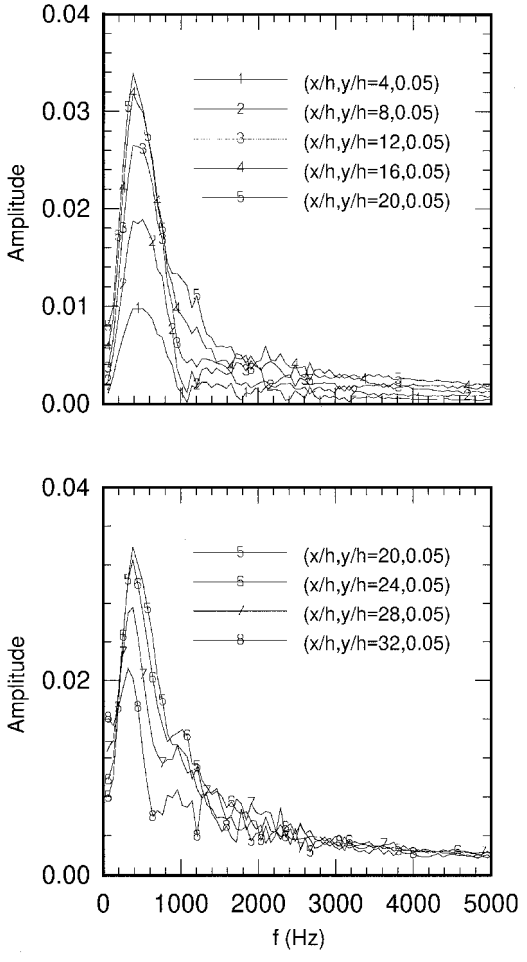


**Fig. 13 Near-wall power spectrum profiles of axial velocity fluctuation at various $x/h$ along $y/h$ = 0.05 ($\tilde{v}_w$ = 3.1 m/s).**

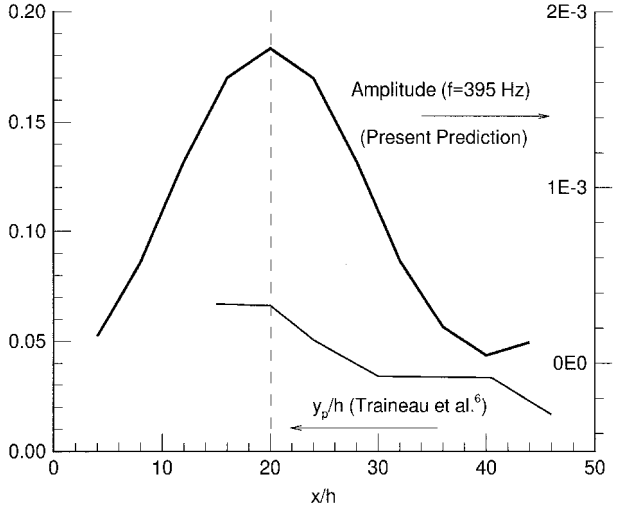


**Fig. 14 Streamwise variation of predicted power-spectrum peak amplitude of near-wall axial velocity fluctuations and measured transverse location of maximum in turbulence intensity ($\tilde{v}_w$ = 3.1 m/s).**

there exists a critical location, $x/h$ = 20, at which the power spectrum peak amplitude is the maximum among the near-wall locations investigated. Furthermore, the present predicted critical location for the maximum peak amplitude of near-wall velocity-fluctuation power spectrum is found to coincide with the measured critical location for the turbulence-intensity transition by Traineau et al.,[6] as depicted in Fig. 14. The present study can thus provide a physical explanation for the occurrence of turbulence-intensity transition. That is, the turbulence-intensity transition occurs at a location where the fluctuating motion is the most energetic, a finding not reported in the past.

## Conclusions and Future Prospects

The significant effects of injected-fluid turbulence level $\sigma_w$ and compressibility on the flow transitions in a simulated nozzleless SRM with uniform wall injection have been demonstrated computationally by solving the time-dependent compressible Navier–Stokes equations with a subgrid-scale turbulence model. Some key conclusions under the conditions investigated are as follows:

1) The turbulence-intensity transition related to the erosive burning phenomena is found to be sensitive to the level of $\sigma_w$; a $\sigma_w$ as low as 0.01 is sufficient to trigger the turbulence-intensity transition; the turbulence intensity transition advance increases with increasing $\sigma_w$ as $\sigma_w \geq 0.01$.

2) The viscosity effects are found to have no influence on the mean-flow transition.

3) The compressibility by itself alone ($\sigma_w = 0$) can provoke the mean-velocity transition in an SRM as the mean centerline Mach number approaches a critical value of 0.5 (or the mean cross-sectional averaged Mach number reaches 0.33) or the fractional mean density variation attains 12%.

4) The mean-flow transition is found to occur at a fixed axial station independent of the $\sigma_w$ level and is primarily controlled by the compressibility for the injected fluids with a low turbulence level in the range of $0 \leq \sigma_w \leq 0.3$. Beyond $\sigma_w = 0.3$, the effect of $\sigma_w$ becomes dominant and the spatial advance of the mean-flow transition increases or the corresponding critical centerline Mach number decreases with increasing $\sigma_w$.

5) For a porous duct with an appropriate length, three kinds of transition phenomena can be observed according to the range of $\sigma_w$ level and the exit centerline Mach number $(M_{CL})_e$. For $0.01 \leq \sigma_w \leq 0.3$ and $(M_{CL})_e < 0.5$, only a single turbulence-intensity transition is present. For $0.3 \leq \sigma_w \leq 0.9$, both turbulence-intensity and mean-velocity transitions exist; however, the mean-velocity transition lags behind the turbulence-intensity transition. For $\sigma_w = 0.9$, the onsets of the turbulence-intensity and mean-velocity transitions are concurrent. These findings are useful for explaining various transition phenomena reported by other researchers.

6) The near-wall power spectra of velocity fluctuations can well identify the critical location and provide a physical explanation for the onset of turbulence-intensity transition, a finding not reported in the open literature.

There are still more works worthy of study. For instance, the effects of nonuniform wall injection on the flow transitions in an SRM will be investigated in the future. To account for the effects of the vortex stretch on the evolution of the ring vortex shedding from boundary separation in the head-end region, a three-dimensional computation needs to be performed in future work.

## Acknowledgment

This research was supported by the National Science Council of the Republic of China under Contract NSC85-2212-E-007-025.

## References

[1]Liou, T. M., and Lien, W. Y., "Numerical Simulations of Injection-Driven Flows in a Two-Dimensional Nozzleless Solid-Rocket Motor," *Journal of Propulsion and Power*, Vol. 11, No. 4, 1995, pp. 600–606.

[2]Dunlap, R., Willoughby, P. G., and Hermsen, R. W., "Flowfield in the Combustion Chamber of a Solid Propellant Rocket Motor," *AIAA Journal*, Vol. 12, No. 12, 1974, pp. 1440–1442.

[3]Yamada, K., Goto, M., and Ishikawa, N., "Simulative Study on the Erosive Burning of Solid Rocket Motors," *AIAA Journal*, Vol. 14, No. 9, 1976, pp. 1170–1176.

[4]Taylor, G. I., "Fluid Flow in Regions Bounded by Porous Surfaces," *Proceedings of the Royal Society of London*, Series 234A, Vol. 1199, 1956, pp. 456–475.

[5]Culick, F. E. C., "Rotational Axisymmetric Mean Flow and Damping of Acoustic Waves in Solid Propellant Rocket Motors," *AIAA Journal*, Vol. 4, No. 8, 1966, pp. 1462–1464.

[6]Traineau, J. C., Hervat, P., and Kuentzmann, P., "Cold-Flow Simulation of a Two-Dimensional Nozzleless Solid-Rocket Motor," AIAA Paper 86-1447, June 1986.

[7]Tsai, G. S., "Effect of Porosity on the Flow Characteristics in Porous Duct with One End Closed," M.S. Thesis, Power Mechanical Engineering Dept., National Tsing Hua Univ., Taiwan, ROC, 1992.

[8]Beddini, R. A., "Injection-Induced Flows in Porous-Walled Ducts," *AIAA Journal*, Vol. 24, No. 11, 1986, pp. 1766–1773.

[9]Sabnis, J. S., Gibeling, H. J., and McDonald, H., "Navier-Stokes Analysis of Solid Propellant Rocket Motor Internal Flows," *Journal of Propulsion and Power*, Vol. 5, No. 6, 1989, pp. 657–664.

[10]Dunlap, R., Blackner, A. M., Waugh, R. C., Brown, R. S., and Willoughby, P. G., "Internal Flow Field Studies in a Simulated Cylindrical Port Rocket Chamber," *Journal of Propulsion and Power*, Vol. 6, No. 6, 1990, pp. 690–705.

[11]Balakrishnan, G., Liñán, A., and Williams, F. A., "Rotational Inviscid Flow in Laterally Burning Solid-Propellant Rocket Motors," *Journal of Propulsion and Power*, Vol. 8, No. 6, 1992, pp. 1167–1176.

[12]Liou, T. M., Lien, W. Y., and Tsai, G. S., "Experimental and Computational Studies of Fluid Flow in a Two-Dimensional Porous-Walled Channel," *9th Symposium on Turbulent Shear Flows* (Kyoto, Japan), 1993, pp. 5-4-1–5-4-6.

[13]Smagorinsky, J., "General Circulation Experiments with the Primitive Equations," *Monthly Weather Review*, Vol. 91, No. 3, 1963, pp. 99–164.

[14]Godunov, S. K., "A Finite Difference Method for the Numerical Computation of Discontinuous Solutions of the Equations of Fluid Dynamics," *Mathematics Sbornik*, Vol. 47, 1959, pp. 271–290.

[15]Liou, T. M., Lien, W. Y., and Hwang, P. W., "A Modified Godunov's Scheme for Shock Tube Flows and Turbulent Combustion Flows," *The 4th National Conference on Combustion Science and Technology*, The Combustion Inst. of ROC, Hsinchu, Taiwan, ROC, 1994, pp. 242–247.

[16]Ragab, S. A., and Sheen, S. C., "Large Eddy Simulation of Mixing Layers," *Large Eddy Simulation of Complex Engineering and Geophysical Flows*, edited by B. Galperin and S. A. Orszag, Cambridge Univ. Press, New York, 1993, pp. 255–285.

[17]Tsai, M. K., and Liou, T. M., "Study of Flow Induced by Nonuniform Lateral Injection," *Journal of Propulsion and Power*, Vol. 7, No. 5, 1991, pp. 668–678.